SCIENTIFIC Publishing Limited

Journal of Hydrological Ecology and Water Security
https://ojs.ukscip.com/index.php/jhews

Article

The Influence of Recurrent Modes of Climate Variability on Intensity and Temporal Phase of Local Hydroclimatic Variation in South Carolina

Donghyun Lee

Future Engineers Team, South Carolina Lexington H. School, Lexington, SC 29072, USA;
leedonghyun@lexington1.net

Received: 25 January 2025; **Revised:** 20 March 2025; **Accepted:** 27 March 2025; **Published:** 5 April 2025

Abstract: Understanding how large-scale climate circulation influences hydroclimatic factors in both tropical and extratropical regions is crucial. This study employed empirical methods to identify areas with consistent hydroclimatic signals associated with the El Niño/Southern Oscillation (ENSO). We examined the climatic linkages between the warm and cold phases of ENSO and precipitation patterns across South Carolina. Spatial coherence values were calculated using monthly precipitation composites over a 2-year ENSO cycle, and candidate regions were identified using the first harmonic fit. Temporal consistency rates were determined through aggregate composites and index time series (ITS) to pinpoint core regions. This study identified three core regions: the Upstate Region (USR), the Pee-Dee Region (PDR), and the Lowcountry Region (LCR), with the LCR showing the most significant response to both warm and cold ENSO forcings. During ENSO warm (cold) years, precipitation composites showed above (below) normal levels in these regions from winter to spring. Spatial coherence rates for El Niño (La Niña) in USR, PDR, and LCR were between 0.96 and 0.98 (0.95 and 0.97), and temporal consistency rates ranged from 0.72 to 0.83 (0.73 to 0.77). Composite-harmonic analysis revealed that precipitation anomalies tend to reverse signs between opposite ENSO phases, with positive anomalies in warm years showing more coherence and stronger responses compared to negative anomalies in cold years. The findings indicate that South Carolina's precipitation patterns are significantly influenced by ENSO, highlighting a climatic teleconnection between large-scale climate circulation and middle latitude precipitation.

Keywords: Precipitation; Teleconnection; Climatic Impact; Hydroclimatology

1. Introduction

El Niño, which means "Little Boy" in Spanish, occurs due to weakened trade winds leading to the warming of sea surface temperatures in the Equatorial Pacific, including central and eastern tropical regions. This warming causes warm water to reach the western coast of the Americas, shifting the Pacific jet stream southward and resulting in increased flooding and rainfall in the Southeast United States, along with drier conditions in the northern U.S. Conversely, La Niña, meaning "Little Girl" in Spanish, involves the cooling of sea surface temperatures in the central and eastern tropical Pacific as strong trade winds push warm water westward toward Asia. This cooling often leads to upwelling along the western coast of the Americas, causing floods and droughts worldwide. The Southern Oscillation (SO) is a bimodal variation in sea level barometric pressure between two observation stations, which measures the atmospheric pressure difference between Darwin, Australia, and Tahiti, French Polynesia. It is derived from the monthly average pressure anomalies at these two sites. In addition, the El Niño/Southern Oscillation

(ENSO) is linked to sea surface temperature differences in the Equatorial Pacific, affecting the eastern-central Pacific Ocean as a recurring climate pattern. The ENSO cycle, lasting from 1 to 7 years, involves temperature variations of 1 to 3 degrees, with El Niño and La Niña representing its extreme phases [1].

Numerous studies have examined these phenomena on global and regional scales, exploring naturally occurring events. Consequently, these investigations have amassed extensive information on the effects of ENSO, including major hydrological extremes like floods and droughts worldwide. This data has facilitated the development of various scientific methods to predict and prepare for hazardous events such as droughts, floods, and rainstorms. The Southern Oscillation's impact on Indian rainfall was first studied by Walker et al. [2,3]. Since then, many global studies have explored ENSO's extreme phases, identifying significant links between these phases and global precipitation patterns. Berlage [4] found a strong correlation between ENSO extreme events and global precipitation anomalies, while Rasmusson and Carpenter [5] linked Southern Oscillation phases to precipitation and temperature patterns. Ropelewski et al. [6,7] examined spatiotemporal ranges, finding consistent global precipitation responses to both ENSO extreme phases. Kiladis and Diaz [8] confirmed these strong correlations between ENSO phases and precipitation anomalies. Additionally, to investigate the temporal patterns of maximum daily precipitation, Westra et al. [9] employed a generalized extreme value analysis (GEV) and found a significant linkage to average global surface air temperature patterns.

Numerous regional studies have demonstrated the impact of ENSO on low- and middle-latitude climatic variabilities, including those by Douglas et al. [10], Rasmusson et al. [11], Ropelewski et al. [12], Redmond et al. [13], and Kahya et al. [14]. Several studies have shown a correlation between ENSO phases and precipitation on a midlatitude regional scale. In the United States, Douglas et al. [10] found that extreme ENSO forces increase Southeastern precipitation in winter. Ropelewski et al. [12] explored the climatic linkages between North American precipitation patterns and the extreme Southern Oscillation, revealing ENSO-related patterns, a finding supported by Kiladis et al. [8]. Regional monthly precipitation anomalies over southern Brazil were examined in association with extreme phases of the Southern Oscillation (SO) by Grimm et al. [15]. Karabörk et al. [16] identified areas in Turkey where precipitation anomalies statistically correlated with both ENSO phases. Jin et al. [17] analyzed the effects of ENSO on precipitation patterns in Korea and Japan, using categorized Southern Oscillation Indexes (SOI) and lead-lag correlation analysis. Chandimala and Zubair [18] studied the Kelani River basin in Sri Lanka, focusing on the climatic linkages among precipitation probability, ENSO episodes, and sea-surface-temperature (SST) using principal component analysis. Power et al. [19] used a coupled general circulation model to investigate the impact of ENSO on Australian precipitation patterns. Cai et al. [20] studied the effects of ENSO forcing on Australian precipitation, documenting the variability of tropical/extratropical precipitation associated with variations in tropical Pacific sea surface temperatures. Lee et al. [21] examined ENSO-related hydroclimatic signals using monthly midlatitude precipitation anomalies, while Wang et al. [22] studied ENSO's effect on the relationship between tropical cyclones and precipitation patterns in China.

As demonstrated, numerous studies have investigated ENSO on global and regional scales. Despite extensive research into ENSO-related climate teleconnections, there is limited knowledge about ENSO events on localized precipitation variation. Recently, precipitation has become more intense and localized, leading to devastating effects, including hydrologic extremes that impact both the natural environment and human life and property. Analyzing how extreme phases of climatic variation influence local precipitation patterns is essential for predicting and preparing for hydroclimatic extremes. Accordingly, it is essential to systematically investigate how the extreme phases of ENSO events—El Niño and La Niña—influence local precipitation variability in South Carolina. This study seeks to provide updated hydroclimatic insights regarding the spatial and temporal extent and intensity of ENSO-induced precipitation signals across different regions of the state. The central objective is to analyze precipitation variability in relation to ENSO extremes using both composite and harmonic analysis techniques. This research assesses the strength, timing, and geographic scope of the ENSO-precipitation relationship by exploring seasonal cycles and spatial distribution patterns. Furthermore, the study offers a comparative assessment of teleconnections associated with the warm and cold phases of ENSO, emphasizing the magnitude and seasonal timing of climatic signals through cross-correlation and annual cycle analyses.

2. Methodological Approaches

2.1. Data and Analysis

This study analyzes monthly precipitation records from 46 climate divisions across South Carolina, obtained from the National Centers for Environmental Information (NCEI), a branch of NOAA responsible for climate data management in the U.S. (**Figure 1**).

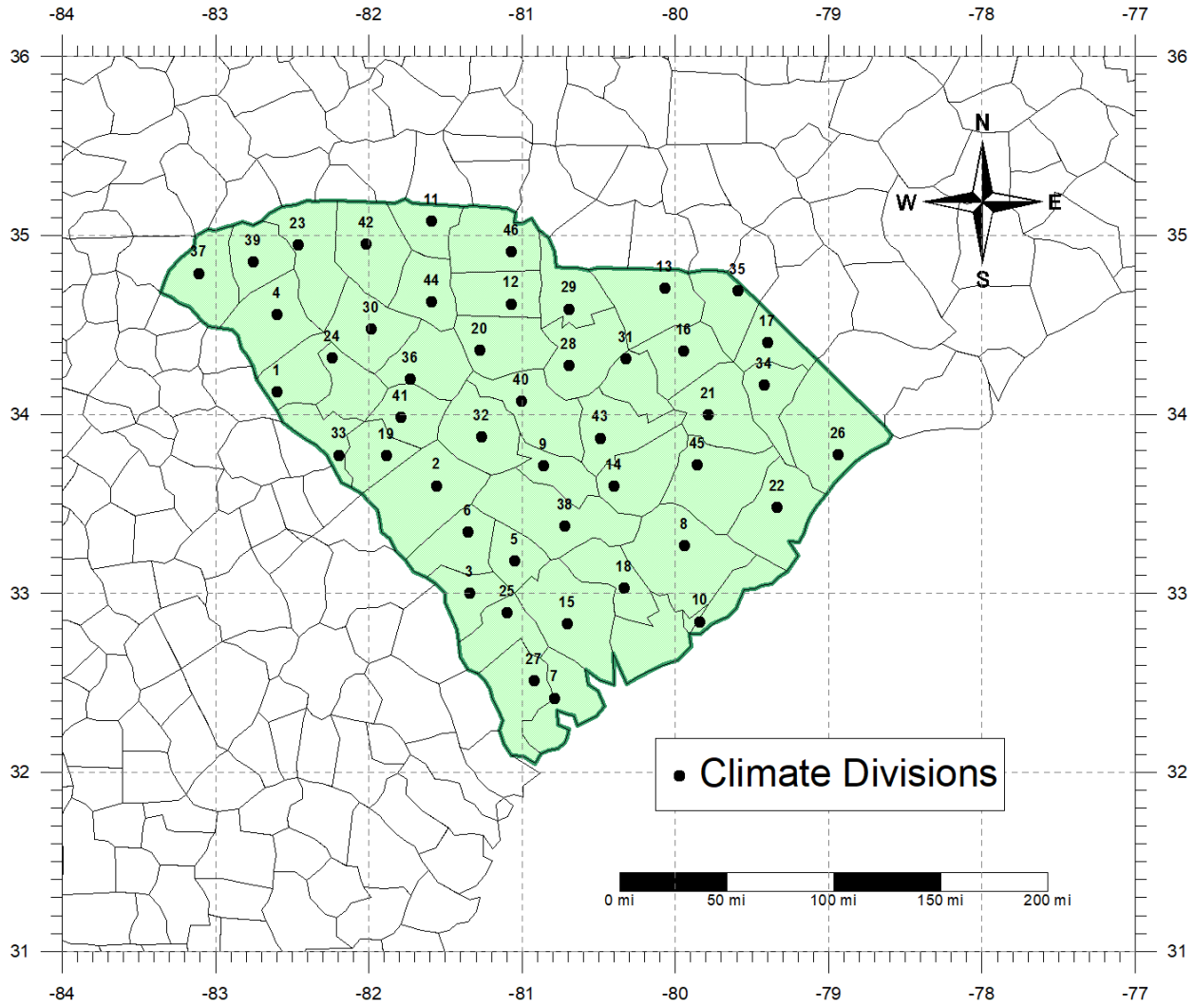

Figure 1. Climate divisions for precipitation indices.

The dataset spans from 1895 to 2020 and encompasses 29 El Niño and 22 La Niña episodes, reflecting the extreme phases of historical ENSO activity. To evaluate the consistency of ENSO-related precipitation anomalies across the state, two distinct sets of ENSO events—El Niño and La Niña—were selected based on classification criteria established by Ropelewski et al. [6, 7], Rasmusson et al. [5], and Kiladis et al. [8], as outlined in **Table 1**(A). The Southern Oscillation Index (SOI), sourced from NOAA's Climate Prediction Center, is used to represent large-scale climatic fluctuations in the central and eastern Pacific Ocean. The SOI is calculated from standardized sea level pressure differences between Darwin and Tahiti, serving as a key indicator of ENSO phases.

Table 1. Overall results of harmonic analysis, hypergeometric analysis, and cross-correlation analysis.

Classification			El Niño Events			La Niña Events		
A. ENSO Event Years			1905, 1911, 1914, 1918, 1923, 1925, 1930, 1932, 1939, 1941, 1951, 1953, 1957, 1963, 1965, 1969, 1972, 1976, 1982, 1986, 1991, 1994, 1997, 2002, 2004, 2006, 2009, 2015, 2018			1910, 1915, 1917, 1924, 1928, 1938, 1950, 1955, 1964, 1971, 1973, 1975, 1985, 1988, 1995, 1998, 2000, 2005, 2007, 2010, 2011, 2017		
			Total: 29			Total: 22		
B. Harmonic Analysis								
	Core Regions		USR	PDR	LCR	USR	PDR	LCR
	Signal Season		Sep(0)–Jan(+)	Oct(0)–Feb(+)	Nov(0)–Mar(+)	Oct(0)–Apr(+)	Nov(0)–Apr(+)	Nov(0)–May(+)
	Coherence Rates		0.98	0.96	0.97	0.96	0.97	0.95
	Total Episodes		29	29	29	22	22	22
	Occurrence Episode		23	21	24	17	16	17
	Consistency Rates		0.79	0.72	0.83	0.77	0.73	0.77
	Extreme Events		11	11	12	7	8	7
C. Hypergeometric Analysis								
	Case I	**N**	125	125	125	125	125	125
		k	66	62	59	65	60	59
		n	29	29	29	22	22	22
		m	23	21	24	17	16	17
		Prob.	0.001	0.003	0.000	0.006	0.010	0.002
	Case II	**N**	125	125	125	125	125	125
		k	25	25	25	25	25	25
		n	25	25	25	22	22	22
		m	11	11	12	7	8	7
		Prob.	0.002	0.002	0.001	0.031	0.039	0.031
D. Cross-Correlation Analysis								
	Strong Warm Phase	**lag-0**	−0.01	0.27	0.19	−0.02	0.27	0.14
	(α = 0.05)	**lag-1**	**0.30**	0.01	−0.18	**0.37**	−0.03	−0.11
		lag-2	**−0.69**	**−0.55**	**−0.57**	**−0.69**	**−0.53**	**−0.61**
		lag-3	**−0.84**	**−0.75**	**−0.83**	**−0.83**	**−0.79**	**−0.83**
		lag-4	**0.43**	0.16	0.16	**0.41**	0.10	0.26
	Normal Condition	**lag-0**	0.03	−0.01	0.02	0.04	−0.01	0.03
	(α = 0.05)	**lag-1**	0.08	0.04	0.07	0.08	0.05	0.07
		lag-2	−0.02	−0.06	−0.06	−0.02	−0.06	−0.05
		lag-3	0.03	0.03	0.02	0.04	0.02	0.02
		lag-4	0.02	0.04	0.04	0.02	0.05	0.03
	Strong Cold Phase	**lag-0**	**0.57**	**0.47**	**0.52**	**0.52**	**0.46**	**0.56**
	(α = 0.05)	**lag-1**	**−0.52**	−0.14	−0.02	**−0.49**	−0.08	−0.14
		lag-2	**0.56**	**0.66**	**0.71**	**0.59**	**0.66**	**0.68**
		lag-3	−0.07	−0.28	0.16	−0.14	−0.19	0.17
		lag-4	**0.47**	**0.55**	**0.50**	**0.45**	**0.53**	**0.50**

To explore how extreme ENSO forcing influences precipitation patterns across the proposed area, this study applies empirical methods employed by Ropelewski and Halpert [12], including cross-correlation analysis and annual cycle analysis, with modifications and enhancements. Correlation coefficients between the categorized SOI and percentile-ranked precipitation time series are calculated using Spearman's cross-correlation analysis with a statistical significance level of 0.05. **Figure 2** outlines the analysis process in three stages: initial data processing to convert raw data into appropriate formats like ranked percentiles, modular coefficients, and categorized SOIs; followed by the identification of core regions through composite and harmonic analyses, and concludes with a comparative assessment of ENSO-related precipitation signals using annual cycle and lead-lag correlation analyses. For the annual cycle analysis, monthly precipitation values are converted into modular coefficients, a transformation that removes variance and mean effects to standardize the data. These coefficients represent precipitation as a percentage of the annual mean, ensuring uniform cyclic patterns across all climate divisions. Seasonal lead-lag correlation coefficients are then calculated between precipitation percentiles and categorized SOI values. Four seasonal groupings are defined—December–February, March–May, June–August, and September–November—by averaging monthly data within each period. The SOI values are classified into five categories according to their intensity: strong La Niña (cold), weak La Niña, neutral, weak El Niño (warm), and strong El Niño. Seasonal precipitation time series are subsequently converted into percentile-ranked probability values using the Weibull plotting position method. This approach eliminates periodic trends and corrects for variability across climate divisions. Monthly precipitation values are sorted in ascending order and normalized by dividing each rank by (n + 1), where

(n) represents the total number of observations in the dataset.

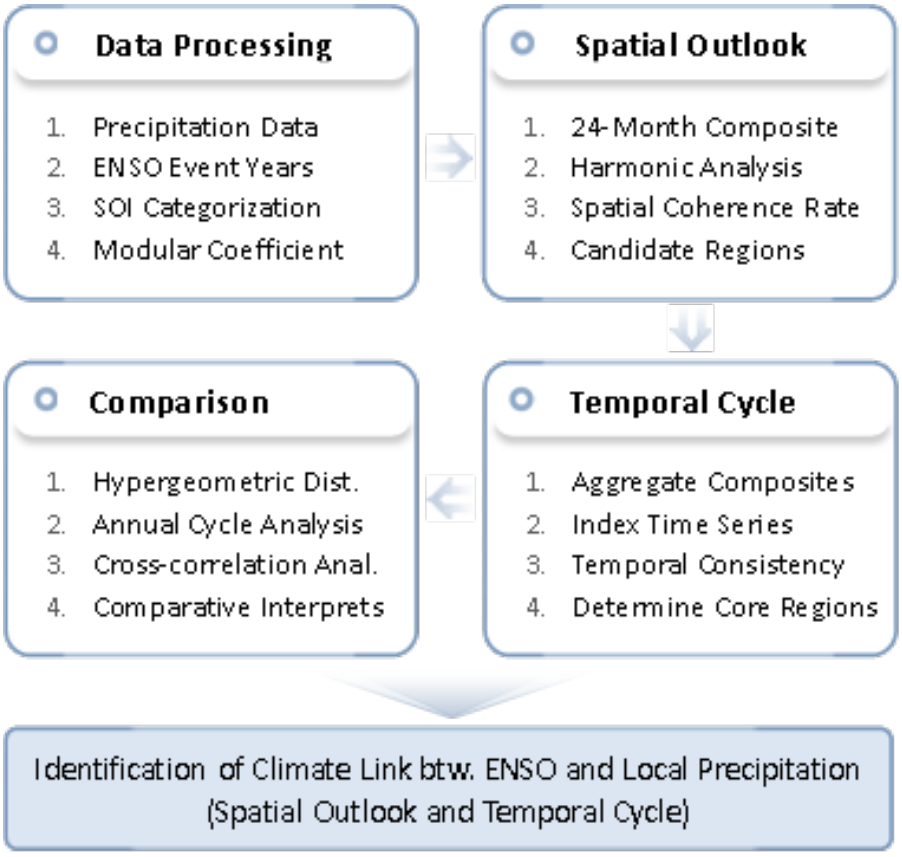

Figure 2. Flowchart of the methodology.

2.2. Composite and Harmonic Analysis

For each climate zone, monthly precipitation percentile composites are computed over 2 years, beginning in July of the year preceding the ENSO event and extending through June of the following year. The starting month is denoted as Jul (–), and the ending month as Jun (+), corresponding to the ENSO high or low phase. The composite is calculated for each SO event, fitting them with the first harmonic of a theoretical 24-month SO period (either warm or cold phases). This approach follows the assumption that a cycle of precipitation anomaly has a high/low point for an extreme event, and the event corresponds to the annual cycle, as illustrated in **Figure 3**.

A 2-year cycle was employed as it encompasses a full cycle of an SO phase [5]. For the first harmonic fit, the amplitude indicates the strength of precipitation responses linked to ENSO, and the peak timing relative to the mean value is represented by the angular phase, as shown in **Figure 3**. The theoretical background of the harmonic fits is based on the Fourier Transform as described in Wilks [23].

$$P_t = \overline{P} + \sum_{i=1}^{n/2} \left\{ C_i \cos\left[\frac{2\pi i t}{N} - \beta_i\right]\right\} = \overline{P} + \sum_{i=1}^{n/2} \left\{ A_i \cos\left[\frac{2\pi i t}{n}\right] + B_i \sin\left[\frac{2\pi i t}{n}\right]\right\} \quad (1)$$

$$A_i = \frac{2}{n}\sum_{t=1}^{n} y_t \cos\left(\frac{2\pi i t}{n}\right), \quad B_i = \frac{2}{n}\sum_{t=1}^{n} y_t \sin\left(\frac{2\pi i t}{n}\right), \quad C_i = \left(A_i{}^2 + B_i{}^2\right)^{0.5} \quad (2)$$

$$\beta_i = \tan^{-1}\frac{B_i}{A_i}\ (A_i > 0), \quad \frac{\pi}{2}\ (A_i = 0), \quad \tan^{-1}\frac{B_i}{A_i} \pm \pi\ (A_i < 0) \quad (3)$$

where P_t and $\overline{P}$ are the monthly and mean precipitation, C_i is the magnitude of the harmonic curve, β_i is the peak time of the harmonic curve, and A_i and B_i are the Fourier coefficients.

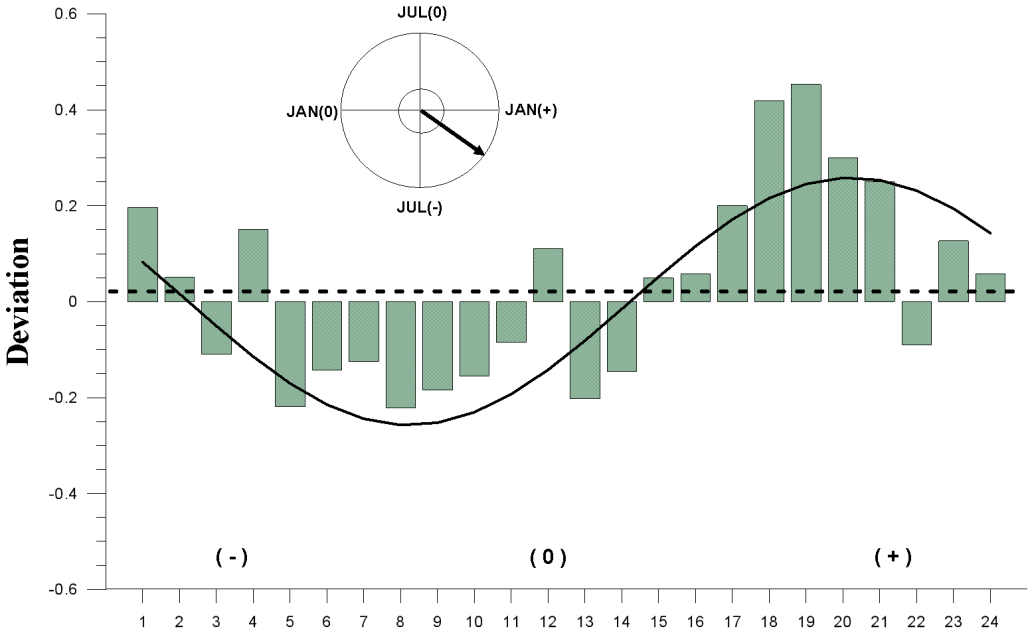

Figure 3. A first harmonic fit to the precipitation ENSO composite for the climate division CD-45. The amplitude and the phase of the first harmonic are presented as a harmonic dial (the upper left).

The temporal phase and amplitude of the harmonic curve are depicted as vectors for each climate division after fitting the climatic division composites with a 24-month harmonic. In this approach, vectors point towards periods of wetter-than-normal precipitation, corresponding to the positive phase of the cycle. The actual direction of the ENSO-precipitation relationship is determined by examining these composites. This study focuses on regions in South Carolina that exhibit significant and sustained ENSO-precipitation correlations over many months. Climate divisions that are not part of the candidate regions are excluded from further consideration. Harmonic vector mapping offers a means of detecting geographic regions that exhibit coherent precipitation responses to ENSO variability. Regions demonstrating the highest coherence were identified by calculating the ratio of their average vector magnitude to the overall mean vector magnitude across all areas.

$$\text{Spatial Coherence} = \frac{\text{sqrt}\left(\left(\sum V\cos\theta\right)^2 + \left(\sum V\sin\theta\right)^2\right)}{\sum V} \tag{4}$$

The denominator contains the arithmetic average value of the vector magnitudes, and the numerator is the average vector magnitude of all harmonic vectors in the chosen regions. V and θ are the magnitude and angle of the vector. This analysis is restricted to areas where coherence values reach or exceed 0.80 [12], excluding regions with high-amplitude but inconsistent phase relationships across climate divisions.

Index Time Series (ITS) were derived by averaging precipitation data both spatially and temporally during key signal seasons, across multiple ENSO years within selected candidate regions. These ITS values serve as indicators of the temporal consistency of ENSO-precipitation relationships. This value was quantified as the proportion of ENSO years in which a clear signal appeared in the ITS, relative to the total number of ENSO events, thereby isolating core regions with stable ENSO-precipitation linkages. The study also investigates extreme precipitation events associated with ENSO, following methods outlined by Ropelewski et al. [12] and Lee et al. [21] to explore the climatic connection between ENSO events and extreme precipitation anomalies. Years with ENSO-related extreme precipitation are identified within signal seasons. Index Time Series (ITS) data are ranked, normalized across the dataset, and converted into probability time series to categorize extreme event levels. The lowest and highest ITS values are assigned probabilities of 20% and 80%, respectively [14].

2.3. Comparative Analyses

Precipitation responses linked to ENSO are assessed using the hypergeometric distribution test. Originally introduced by Haan [24], this statistical test evaluates the probability of observing at least m successful outcomes in n trials from a population of size N, which contains k successes. This cumulative probability serves as an indicator of statistical significance for precipitation anomalies related to warm and cold ENSO phases. Kahya et al. [14] later refined the method to examine not only average conditions but also extreme events—both high and low values. In the present study, two distinct scenarios are analyzed based on the criteria used to define "success". Scenario I considers a year a success if its ITS (Index Time Series) value is either above or below the median in association with ENSO forcing. Scenario II defines success more stringently, identifying years where ITS values fall within the top or bottom 20% of the distribution. To further explore the influence of ENSO on precipitation variability, an annual cycle analysis is conducted, examining how both the trend and magnitude of precipitation anomalies evolve throughout the year. Monthly precipitation data are transformed into modular coefficients, which normalize the series by removing variability due to mean shifts and dispersion. These coefficients express monthly values as percentages relative to the annual mean, allowing for standardized comparison across time and locations. To evaluate ENSO-related precipitation signals seasonally, cross-correlation coefficients are calculated, capturing both positive and negative relationships. Five categorized SOI datasets, representing various ENSO indices correlated with percentile-ranked precipitation time series. Considering atmospheric and oceanic fluctuations, other ENSO indices, such as the Oceanic Niño Index (ONI) and the Multivariate ENSO Index, are considered indicators for tropical ENSO forcing, in addition to the SOI, which is widely used in atmospheric circulation analysis. However, since the ONI and MEI do not cover the precipitation observation period from 1895 to 2020, these indices are not included further. The resulting coefficients reflect both the strength and direction of the climatic connections between ENSO phases and regional precipitation behavior. Additional methodological details regarding data processing and correlation techniques are outlined in the earlier sections of this study.

3. Results

3.1. Results of El Niño Events

Figure 4 presents a harmonic dial map highlighting candidate regions identified through empirical and statistical analyses. The precipitation vector map reveals three spatially coherent regions in the study areas with strong responses to ENSO forcing: the Upstate Region (USR), Pee-Dee Region (PDR), and Lowcountry Region (LCR). Composite precipitation indices for these regions are summarized in **Table 1**(B), reinforcing their sensitivity to ENSO variability. A closer examination of these indices shows that each region experiences distinct seasonal precipitation patterns within the ENSO cycle. **Figure 5** displays the precipitation index time series for the USR, covering the period from September (0) to January (+), and averaged across all stations in the region. This time series shows that 23 out of 29 ENSO events were associated with above-average precipitation. Notably, 11 of these events produced index values at or above the 80th percentile threshold, whereas only one event fell below the 20th percentile. Temporal consistency and spatial coherence for this region were calculated at 0.79 and 0.98, respectively. **Figure 6** shows the corresponding time series for the PDR, from October (0) to February (+). During 21 out of 29 ENSO events, precipitation indices were above average. Eleven ENSO years exceeded the 80th percentile threshold; however, high index values also occurred in 14 non-ENSO years, indicating some overlap. Only two ENSO seasons registered below the 20th percentile. The temporal consistency and spatial coherence for this region were 0.72 and 0.96. **Figure 7** presents the precipitation index time series for the LCR, spanning November (0) to March (+), and reveals a particularly robust ENSO signal. Based on climate division data, 24 out of 29 ENSO events aligned with above-median precipitation. Of these, 12 events exceeded the 80th percentile threshold, providing strong evidence that ENSO acts as a reliable indicator of precipitation anomalies in this region. The LCR also exhibited the highest levels of temporal consistency and spatial coherence, measured at 0.83 and 0.97, respectively.

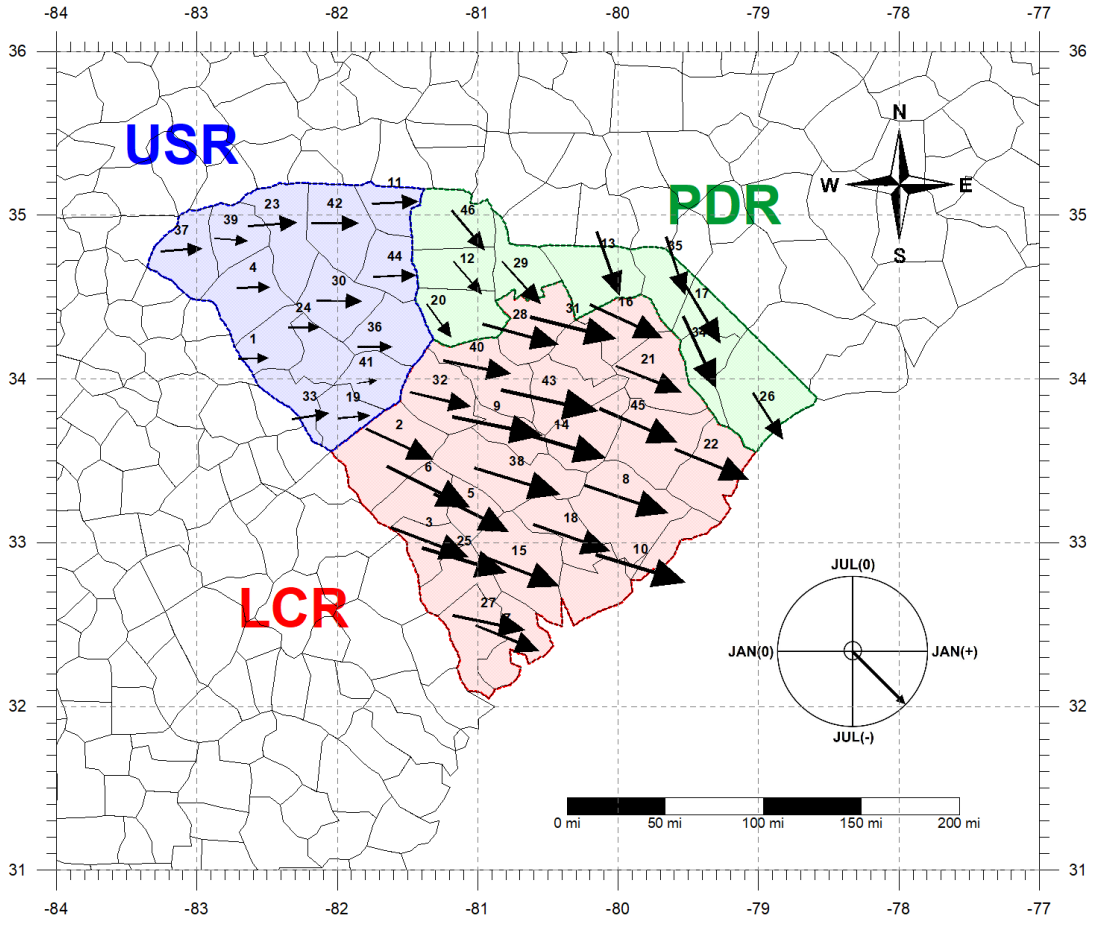

Figure 4. Harmonic dial map based on the first harmonic of the 2-year El Niño composites. Scale for the direction of arrows: south, July(−); west, January(0); north, July(0); and east, January(+). The magnitude of the arrows is proportional to the amplitude of the harmonics.

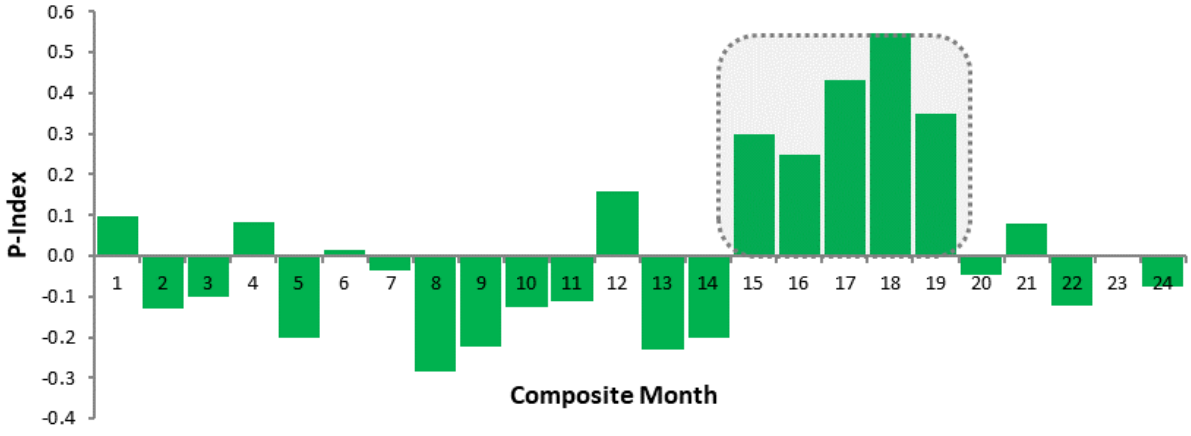

(a)

Figure 5. *Cont.*

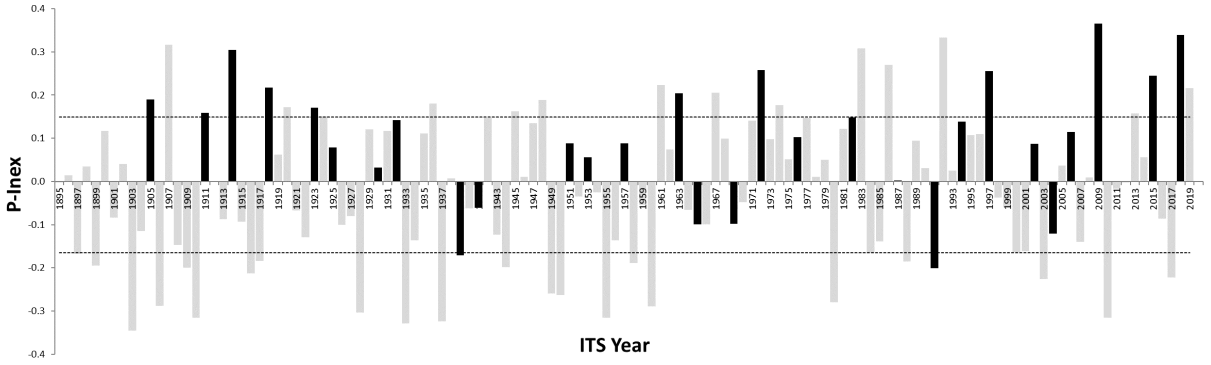

(**b**)

Figure 5. (**a**) El Niño aggregate composite for the candidate US region. The dashed line box delineates the season of possible El Niño-related responses. (**b**) The index time series for the US region for the season previously detected. El Niño years are shown by solid bars. The dashed horizontal lines are the upper (80%) and lower (20%) limits for the distribution of ITS values.

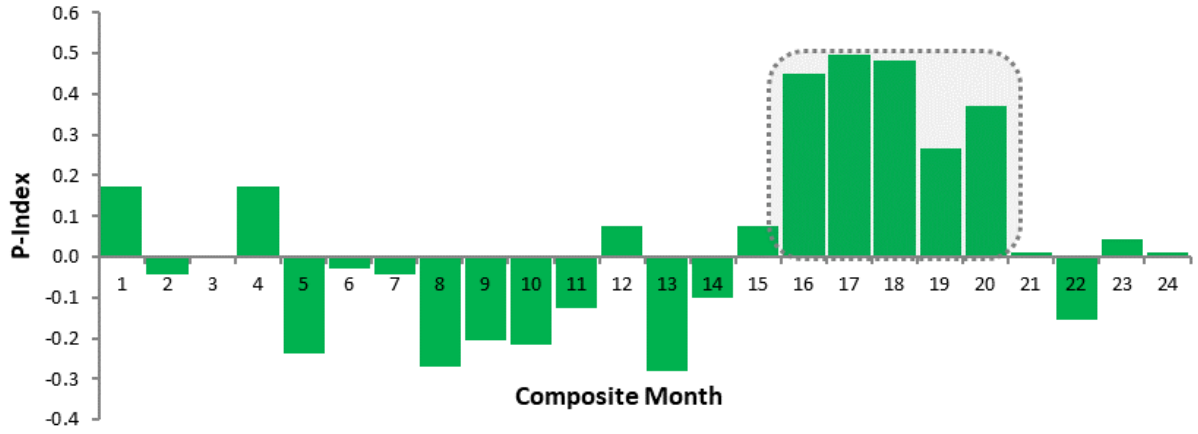

(**a**)

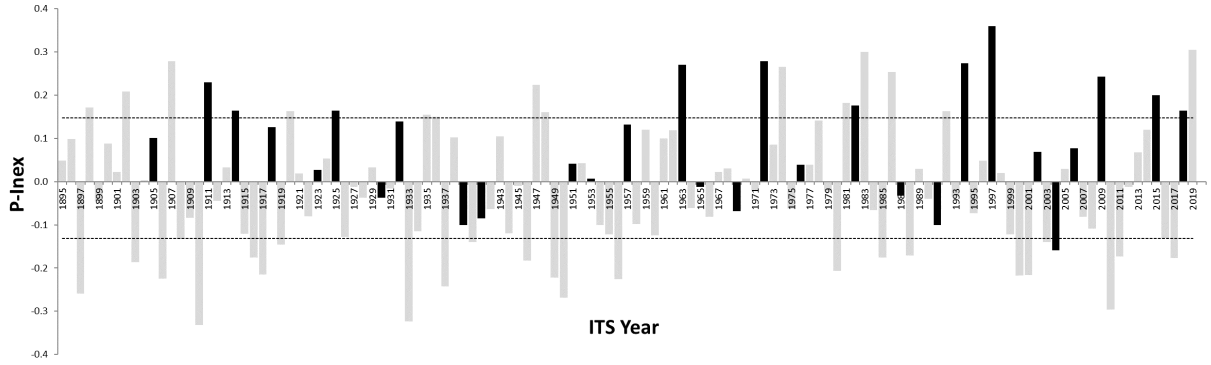

(**b**)

Figure 6. (**a**) El Niño aggregate composite for the candidate PD region. The dashed line box delineates the season of possible El Niño-related responses. (**b**) The index time series for the PD region for the season previously detected. El Niño years are shown by solid bars. The dashed horizontal lines are the upper (80%) and lower (20%) limits for the distribution of ITS values.

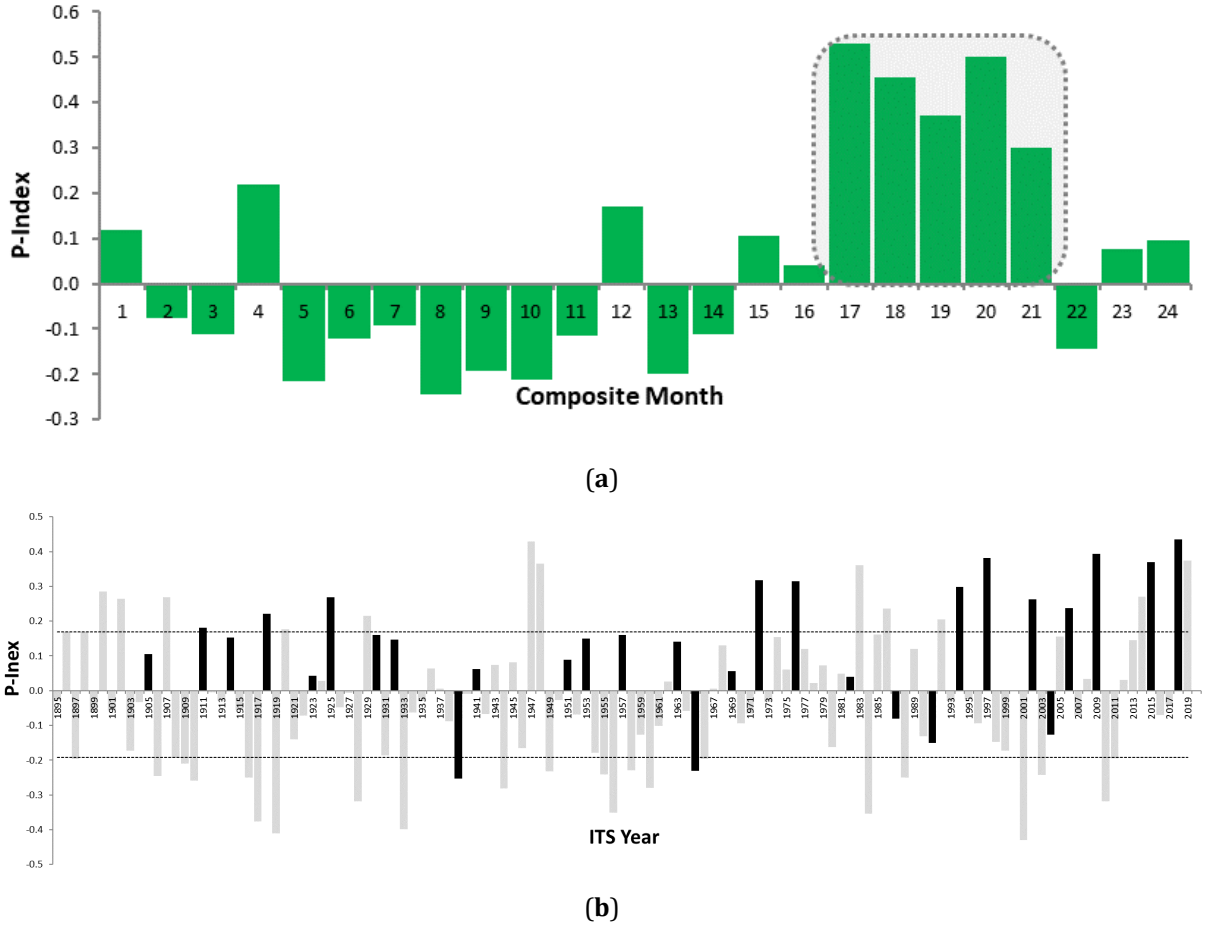

Figure 7. (**a**) El Niño aggregate composite for the candidate LC region. The dashed line box delineates the season of possible El Niño-related responses. (**b**) The index time series for the LC region for the season previously detected. El Niño years are shown by solid bars. The dashed horizontal lines are the upper (80%) and lower (20%) limits for the distribution of ITS values.

3.2. Results of La Niña Events

For the 22 La Niña events—representing the cold phase of the ENSO cycle—monthly precipitation data were analyzed using both composite and harmonic methods. **Figure 8** presents a harmonic dial map illustrating consistent precipitation responses across three regions in South Carolina: the Upstate Region (USR), Pee-Dee Region (PDR), and Lowcountry Region (LCR). **Figures 9** through 11 display ENSO composite precipitation indices for these regions, with summary statistics provided in **Table 1**(B). In the USR, standardized precipitation anomalies, averaged across all climate divisions from October (0) through April (+), show negative departures in 17 of the 22 La Niña events (**Figure 9**). Index values at or below the 20th percentile threshold appeared in 7 La Niña years, while only 2 events exceeded the 80th percentile. The region exhibited high spatial coherence (0.96) and moderate temporal consistency (0.77). In the PDR, analysis of the November (0) to April (+) period revealed below-average precipitation in 16 of the 22 La Niña episodes (**Figure 10**). Eight of these events recorded index values at or beneath the 20% threshold, with none surpassing the 80% mark. Spatial coherence and temporal consistency were 0.97 and 0.73, respectively. The LCR, evaluated from November (0) to May (+), experienced below-median precipitation in 17 out of 22 La Niña years (**Figure 11**). Seven events registered at or below the 20th percentile, while one La Niña season reached or exceeded the 80th percentile threshold. Spatial coherence for this region was 0.95, and temporal consistency stood at 0.77.

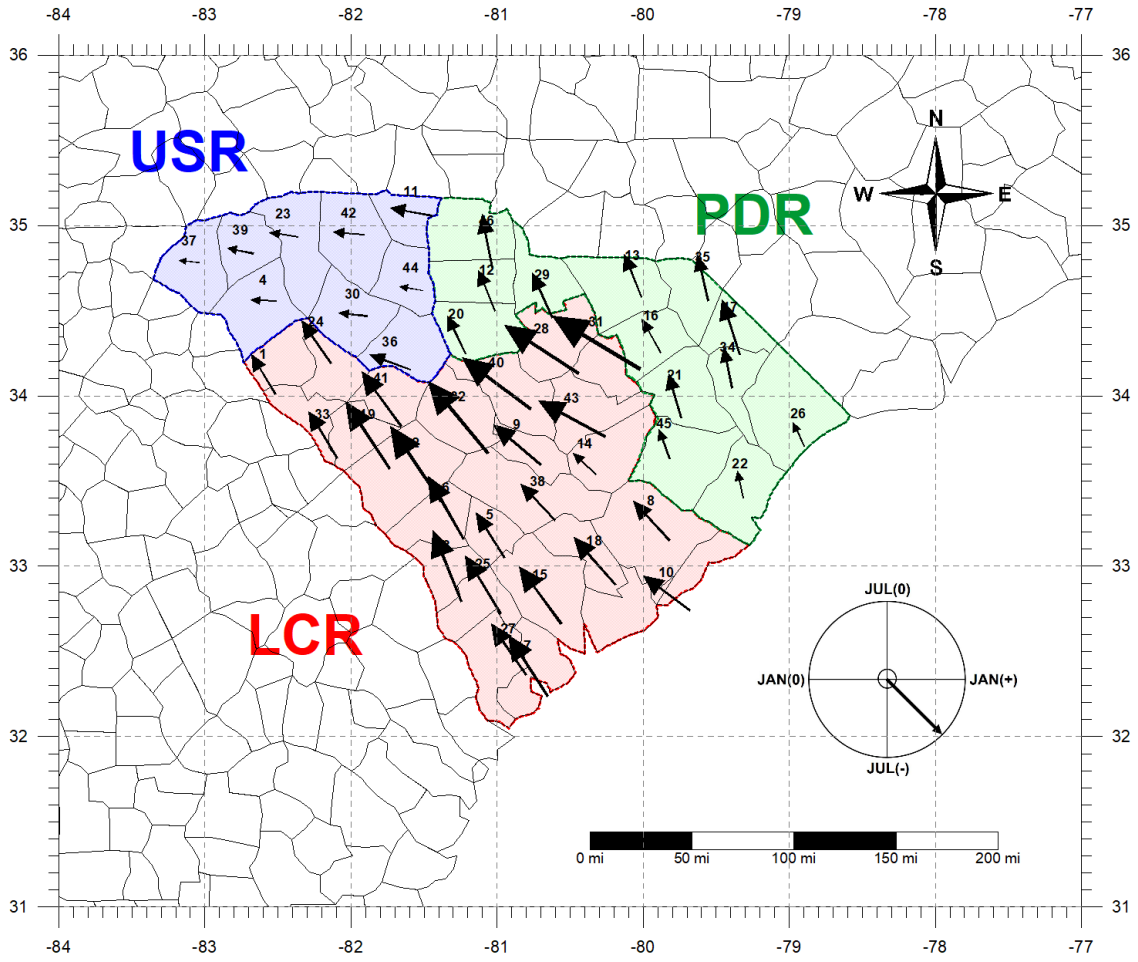

Figure 8. Harmonic dial map based on the first harmonic of the 2-year La Niña composites. Scale for the direction of arrows: south, July(−); west, January(0); north, July(0); and east, January(+). The magnitude of arrows is proportional to the amplitude of the harmonics.

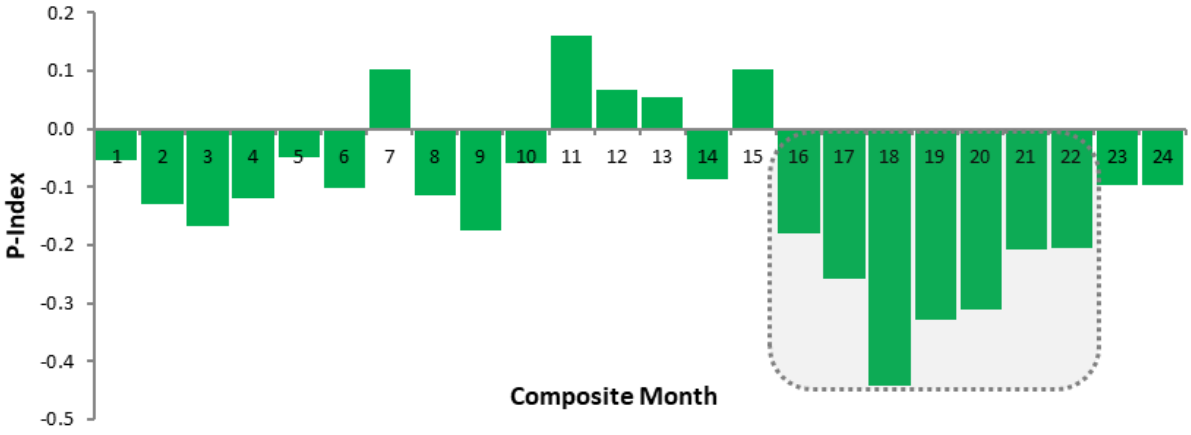

(**a**)

Figure 9. *Cont.*

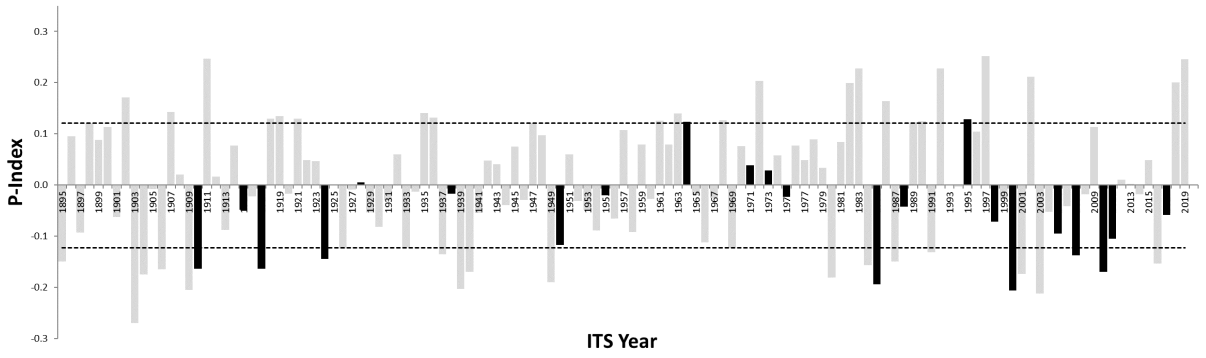

(**b**)

Figure 9. (**a**) La Niña aggregate composite for the candidate US region. The dashed line box delineates the season of possible El Niño-related responses. (**b**) The index time series for the US region for the season previously detected. El Niño years are shown by solid bars. The dashed horizontal lines are the upper (80%) and lower (20%) limits for the distribution of ITS values.

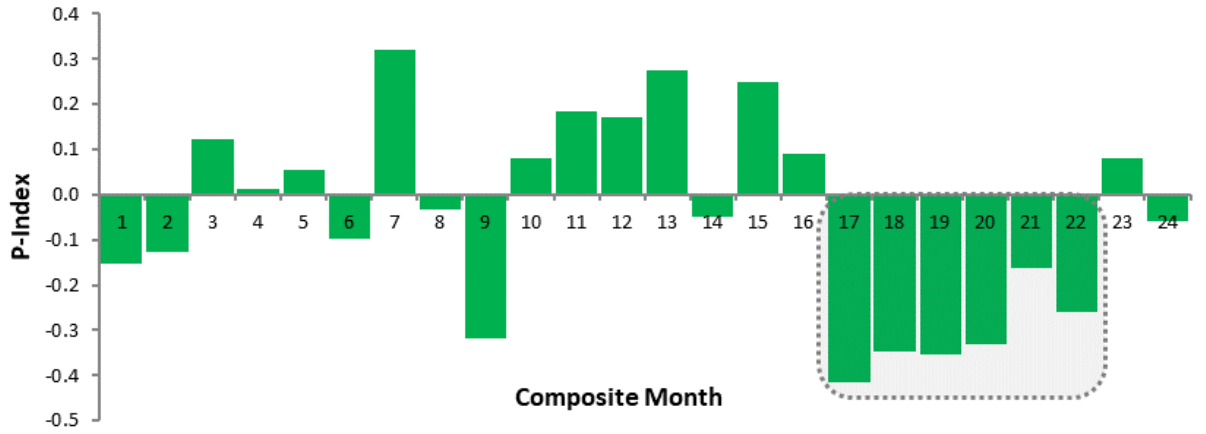

(**a**)

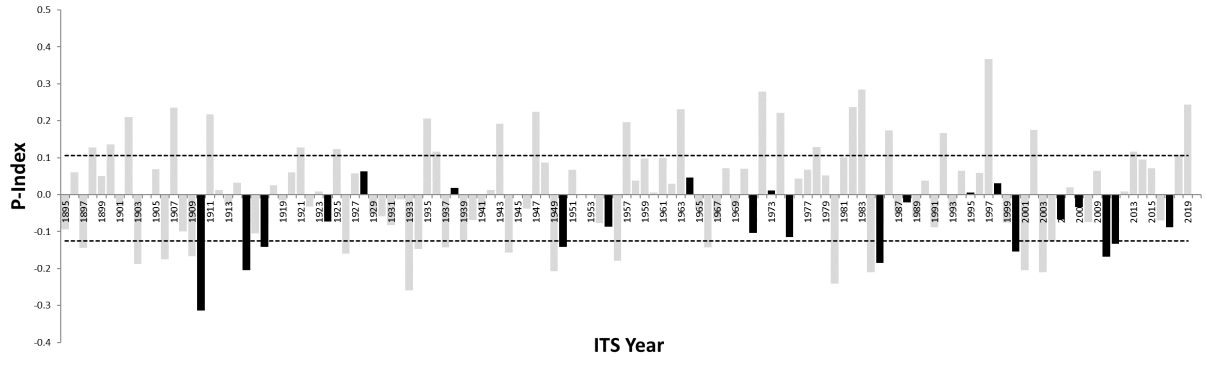

(**b**)

Figure 10. (**a**) La Niña aggregate composite for the candidate PD region. The dashed line box delineates the season of possible El Niño-related responses. (**b**) The index time series for the PD region for the season previously detected. El Niño years are shown by solid bars. The dashed horizontal lines are the upper (80%) and lower (20%) limits for the distribution of ITS values.

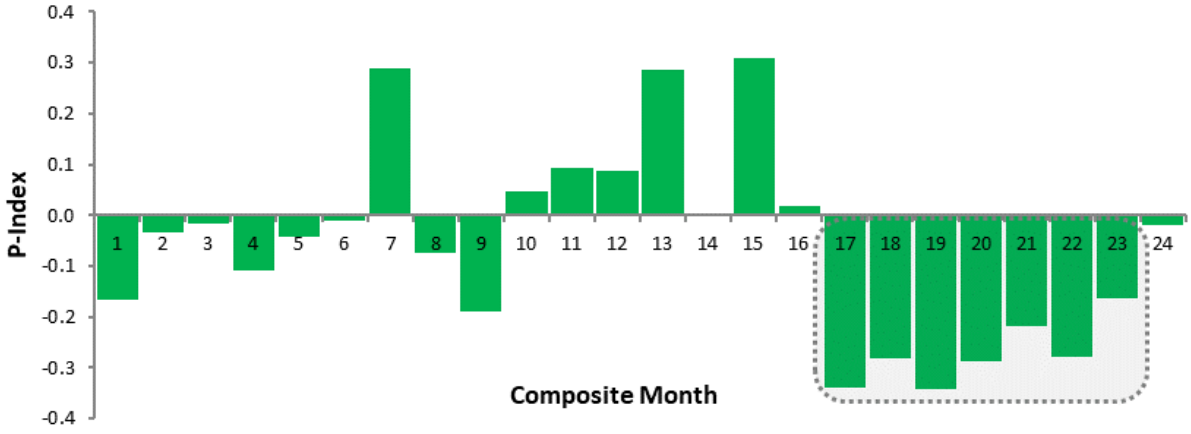

(**a**)

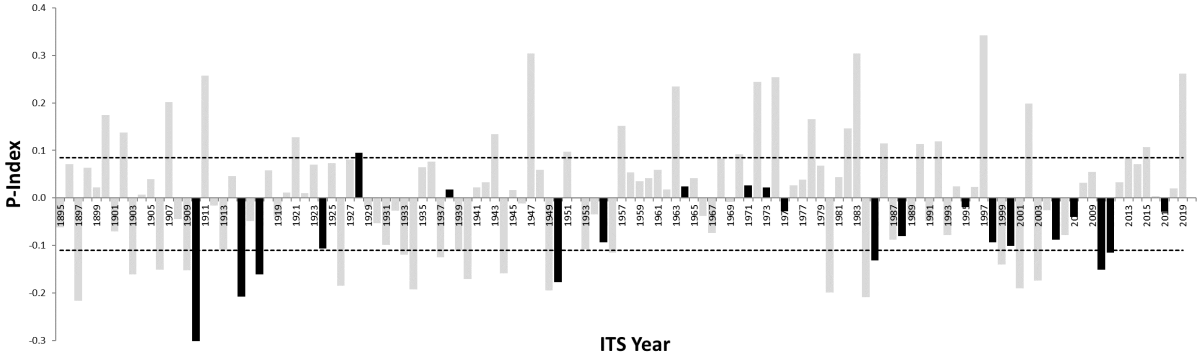

(**b**)

Figure 11. (**a**) La Niña aggregate composite for the candidate LC region. The dashed line box delineates the season of possible El Niño-related responses. (**b**) The index time series for the LC region for the season previously detected. El Niño years are shown by solid bars. The dashed horizontal lines are the upper (80%) and lower (20%) limits for the distribution of ITS values.

3.3. Comparative Analysis Results

The hypergeometric distribution was applied to evaluate the probability that observed wet or dry seasons during ENSO years occurred by chance. In Case I, both ENSO phases yielded extremely low probabilities (below 0.006), suggesting a strong association between ENSO and precipitation anomalies. Case II similarly showed low probabilities for most regions, except La Niña events in the Pee-Dee (PD) region. Over the 125-year study period, extreme wet conditions were found to coincide predominantly with ENSO years. As summarized in **Table 1**(C), the results consistently indicate high temporal consistency rates—ranging from 72% to 83% for El Niño events and from 73% to 77% for La Niña events—demonstrating that the patterns identified in composite analyses are unlikely to be random. Instead, these relationships are likely driven by systematic factors such as tropical sea-surface temperature patterns. Precipitation data were converted into modular coefficients to facilitate analysis of the annual cycle. ENSO composites based on these modular series were plotted against the corresponding regional annual cycles, as illustrated in **Figures 12** and **13**. The figures illustrate two dominant precipitation response patterns linked to ENSO phases. During El Niño events, precipitation tends to be suppressed, followed by an increase in the subsequent year. In contrast, La Niña events are associated with amplified precipitation during the ENSO year, which is then followed by a decline in amplitude in the following year. These fluctuations align with previously identified wet and dry signal seasons across the three key regions—Upstate, Pee-Dee, and Lowcountry. Moreover, a clear divergence in monthly precipitation trends was observed between warm and cold ENSO phases over the full 2-year cycle. These findings suggest that tropical thermal anomalies have a significant influence on the timing and inten-

sity of monthly precipitation in South Carolina, acting as a driver of either wetter or drier conditions. **Table 1**(D) indicates the resultant cross-correlation coefficients, which quantify the strength and direction of the relationship between ENSO forcing and regional precipitation, incorporating five categorized SOI datasets and seasonal time series expressed as percentile-ranked probabilities. Statistically significant correlations ($p < 0.05$) were identified between seasonal precipitation anomalies and both low and high phases of the SOI.

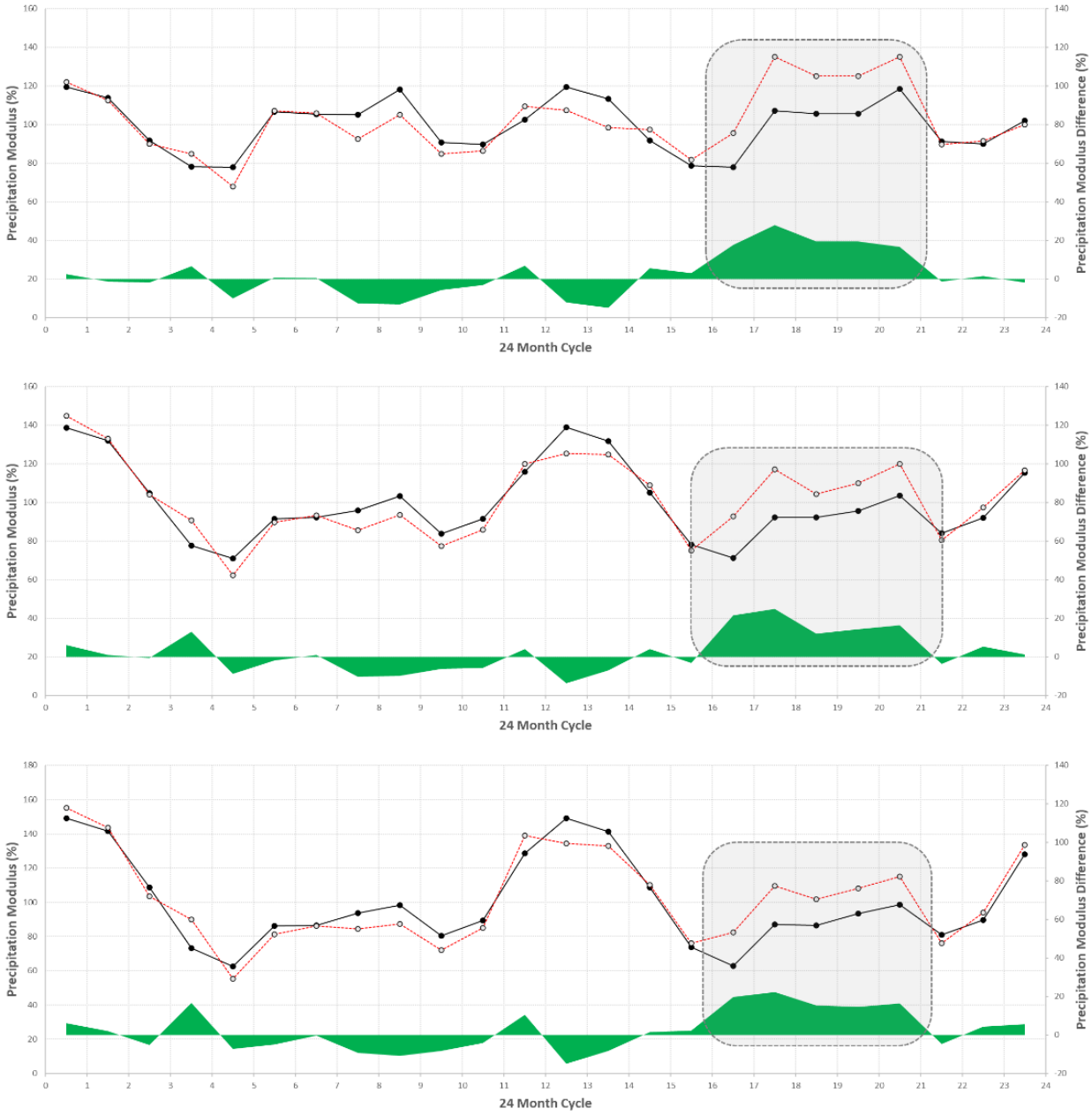

Figure 12. The comparison between El Niño composite cycles (shown by dashed line) and annual cycles (shown by solid line) of the US (upper), PD (middle), and LC (lower) regions, based on modular coefficients. Dashed boxes indicate the beginning and end months of the SO signal season.

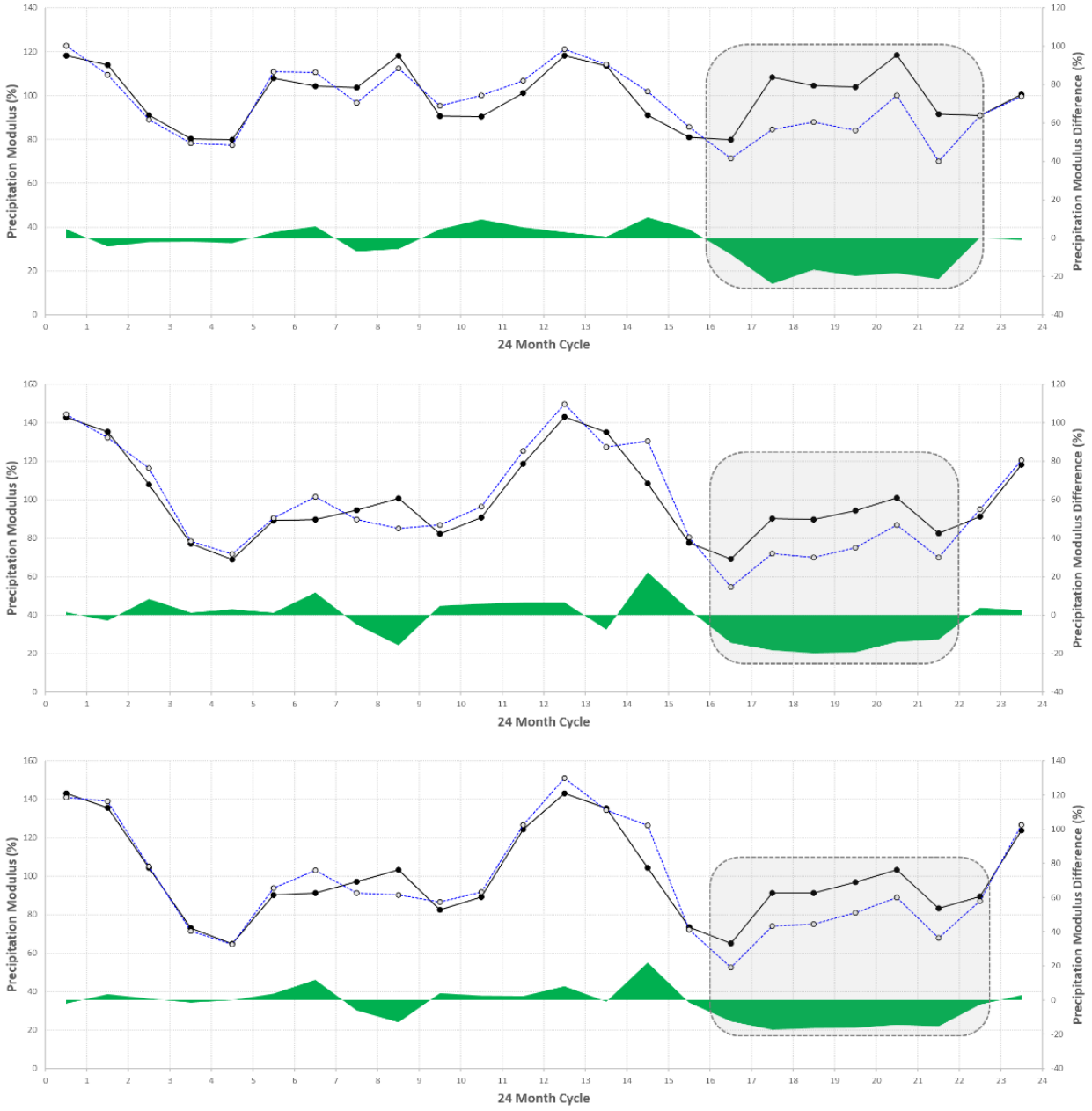

Figure 13. The comparison between La Niña composite cycles (shown by dashed line) and annual cycles (shown by solid line) of the US (upper), PD (middle), and LC (lower) regions, based on modular coefficients. Dashed boxes indicate the beginning and end months of the SO signal season.

It should be noted that ENSO is inversely proportional to SOI. This means that a positive correlation between ENSO and precipitation corresponds to a negative correlation between SOI and precipitation. For strong El Niño (warm SOI) phases, the most prominent positive (negative for SOI) correlation occurred at lag-2 and lag-3 across all three regions, suggesting delayed but strong precipitation increases. In contrast, during La Niña (cold SOI) phases, the strongest negative (positive for SOI) correlations appeared at lag-0, lag-2, and lag-4, indicating that reduced precipitation often coincides with or follows these cold events with varying delays. These patterns confirm that ENSO's influence on South Carolina precipitation operates with a notable lag structure, modulating rainfall increases and decreases according to the strength and timing of tropical Pacific anomalies.

3.4. Discussion

Figures 4 to **7** illustrate that this study identifies increased precipitation during El Niño events in the US, PD, and LC regions in early fall (0) and spring (+) seasons. Particularly in the LC region, the magnitude of this positive deviation from normal precipitation during El Niño years significantly surpasses non-El Niño years. Conversely, **Figures 8** to **11** reveal a contrasting pattern during La Niña, where precipitation indicates below-normal conditions across the US, PD, and LC regions from the previous fall to the following spring. Notably, the negative anomaly during La Niña years in the LC region is markedly higher compared to non-event years. In South Carolina State, the ENSO-related precipitation response aligns with findings by Douglas et al. [10] and Ropelewski et al. [12]. They contended that the impact of ENSO on precipitation patterns is more accurately attributed to direct effects, such as the strengthening of the subtropical jet stream and the warming of Pacific surface waters. Douglas et al. [10] propose that precipitation patterns associated with ENSO could be directly linked to both ENSO itself and the Pacific North American (PNA) teleconnection pattern. Typically, ENSO-induced convection occurs over the southeastern United States, near the equatorial Pacific, which strengthens the westerly winds and leads to increased precipitation and storm activity in the southeastern US, including the Gulf of Mexico [25]. This direct connection to ENSO forcing could help explain the consistent precipitation patterns observed across the southeastern United States. During the peak of ENSO events, Rasmusson and Wallace [11] noted a southward shift in the subtropical jet stream, which had moved from its usual position (1982–1983). This shift intensifies the jet stream and can result in severe winter storms and flooding across the southern US. They also observed that this shift contributed to unusually wet conditions during previous ENSO events in this region. The continual presence of high and low sea-surface temperatures in the eastern-central Pacific Ocean during ENSO events creates large-scale atmospheric circulation patterns through complex ocean-atmospheric interactions. As a result, ENSO-related atmospheric fluctuations in mid-latitude regions contribute to significant precipitation anomalies in South Carolina.

4. Conclusions

Using a combination of statistical and empirical techniques, this study explored the teleconnection between ENSO-induced thermal anomalies and monthly precipitation variability across South Carolina. As outlined in **Table 1**, the study area was delineated into three primary zones: the Upstate Region (USR), the Pee-Dee Region (PDR), and the Lowcountry Region (LCR). These regions exhibited strong spatial coherence and high temporal consistency, underscoring the substantial geographic reach and the ENSO-related impacts on precipitation. Key findings are summarized as follows. For El Niño episodes, precipitation was consistently above average across the US, PD, and LC zones during their respective signal periods—September (0) to January (+) in USR, October (0) to February (+) in PDR, and November (0) to March (+) in LCR. Spatial coherence ranged from 0.96 to 0.98, while temporal consistency varied between 0.72 and 0.83. The LCR displayed the most pronounced positive anomalies for the warm phase of ENSO events. In contrast, La Niña phases were associated with below-average precipitation across the same regions during the dry season windows: October (0) to April (+) in USR, November (0) to April (+) in PDR, and November (0) to May (+) in LCR. Spatial coherence values ranged from 0.95 to 0.97, with temporal consistency rates varying from 0.73 to 0.77.

Furthermore, comparisons between warm and cold ENSO phases revealed inverse precipitation trends—positive precipitation signals for the warm events and negative ones for the cold events. El Niño events were marked by more pronounced above-normal precipitation than the below-normal anomalies seen during La Niña. Annual cycle analysis indicated that fluctuations in South Carolina's precipitation regime are modulated by tropical heating and cooling associated with sea surface temperature anomalies. Cross-correlation results further supported this relationship, showing that the strongest positive (negative) correlations with seasonal precipitation occurred at lags of 2 and 3 seasons (0, 2, and 4 seasons) during strong warm (cold) ENSO phases across all three regions. These findings suggest that stronger ENSO forcing leads to measurable impacts on precipitation, characterized by delayed seasonal responses. In summary, this study demonstrates that ENSO significantly modulates precipitation behavior across South Carolina's mid-latitude regions, producing regionally distinct and seasonally consistent hydrological responses to both ENSO forcings.

Funding

This work received no external funding.

Institutional Review Board Statement

Not applicable.

Informed Consent Statement

Not applicable.

Data Availability Statement

Data retrieved from the National Oceanic and Atmospheric Administration web page.

Conflicts of Interest

The author declares that there is no conflict of interest.

References

1. World Meteorological Organization (WMO). *El Niño/Southern Oscillation*. World Meteorological Organization (WMO): Geneva, Switzerland, 2014.
2. Walker, G.T. Correlation in Seasonal Variations of Weather, VIII. A Preliminary Study of World Weather. *Mem. Indian Meteorol. Dep.* **1923**, *24*, 75–131.
3. Walker, G.T.; Bliss, E.W. World Weather V. *Mem. Roy. Meteor. Soc.* **1932**, *4*, 53–84.
4. Berlage, H.P. The Southern Oscillation and World Weather. *Meteor. Inst. Meded. Verh.* **1966**, *88*, 152.
5. Rasmusson, E.M.; Carpenter, T.H. The Relationship Between Eastern Equatorial Pacific Sea Surface Temperatures and Rainfall Over India and Sri Lanka. *Mon. Wea. Rev.* **1983**, *111*, 517–528.
6. Ropelewski, C.F.; Halpert, M.S. Global and Regional Scale Precipitation Patterns Associated With the El Niño/Southern Oscillation. *Mon. Wea. Rev.* **1987**, *115*, 1606–1626.
7. Ropelewski, C.F.; Halpert, M.S. Precipitation Patterns Associated With the High Index Phase of the Southern Oscillation. *J. Climate* **1989**, *2*, 268–284.
8. Kiladis, G.N.; Diaz, H.F. Global Climatic Anomalies Associated With Extremes in the Southern Oscillation. *J. Climate* **1989**, *2*, 1069–1090.
9. Westra, S.; Alexander, L.V.; Zwiers, F.W. Global Increasing Trends in Annual Maximum Daily Precipitation. *J. Climate* **2013**, *26*, 3904–3918.
10. Douglas, A.E.; Englehart, P.J. On a Statistical Relationship Between Autumn Rainfall in the Central Equatorial Pacific and Subsequent Winter Precipitation in Florida. *Mon. Wea. Rev.* **1981**, *109*, 2377–2382.
11. Rasmusson, E.M.; Wallace, J.M. Meteorological Aspects of the El Niño/Southern Oscillation. *Science* **1983**, *222*, 1195–1202.
12. Ropelewski, C.F.; Halpert, M.S. North American Precipitation and Temperature Patterns Associated With El Niño–Southern Oscillation (ENSO). *Mon. Wea. Rev.* **1986**, *114*, 2165–2352.
13. Redmond, K.T.; Koch, R.W. Surface Climate and Streamflow Variability in the Western United States and Their Relationship to Large Circulation Indices. *Water Resour. Res.* **1991**, *27*, 2381–2399.
14. Kahya, E.; Dracup, J.A. The Influences of Type 1 El Niño and La Niña Events on Streamflows in the Pacific Southwest of the United States. *J. Climate* **1994**, *7*, 965–976.
15. Grimm, A.M.; Ferraz, S.E.T.; Gomez, J. Precipitation Anomalies in Southern Brazil Associated With El Niño and La Niña Events. *J. Climate* **1998**, *11*, 2863–2880.
16. Karabörk, M.Ç.; Kahya, E. The Teleconnections Between Extreme Phases of Southern Oscillation and Precipitation Patterns Over Turkey. *Int. J. Climatol.* **2003**, *23*, 1607–1625.
17. Jin, Y.H.; Kawamura, A.; Jinno, K.; et al. Quantitative Relationship Between SOI and Observed Precipitation in Southern Korea and Japan by Nonparametric Approaches. *J. Hydrol.* **2005**, *301*, 54–65.
18. Chandimala, J.; Zubair, L. Predictability of Streamflow and Rainfall Based on ENSO for Water Resources Management in Sri Lanka. *J. Hydrol.* **2007**, *335*, 303–312.
19. Power, S.B.; Haylock, M.; Colman, R.; et al. The Predictability of Interdecadal Changes in ENSO Activity and ENSO Teleconnection. *J. Clim.* **2006**, *19*, 4755–4771.

20. Cai, W.; van Rensch, P.; Cowan, T.; et al. Teleconnection Pathways of ENSO and the IOD and the Mechanisms for Impacts on Australian Rainfall. *J. Clim.* **2011**, *24*, 3910–3923.
21. Lee, J.H.; Julien, P.Y. Teleconnections of the ENSO and South Korean Precipitation Patterns. *J. Hydrol.* **2016**, *534*, 237–250.
22. Wang, L.; Yang, Z.; Gu, X.; et al. Linkages Between Tropical Cyclones and Extreme Precipitation Over China and the Role of ENSO. *Int. J. Disaster Risk Sci.* **2020**, *11*, 538–553.
23. Wilks, D.S. *Statistical Methods in Atmospheric Sciences*, 3rd ed.; Academic Press: Oxford, UK, 1995.
24. Haan, C.T. *Statistical Methods in Hydrology*; Iowa State University Press: Ames, IA, USA, 1977.
25. Arkin, P.A. The Relationship Between Interannual Variability in the 200 mb Tropical Wind Field and the Southern Oscillation. *Mon. Wea. Rev.* **1982**, *110*, 1393–1404.